# RSC Advances

## MOF-derived Co@C nanoparticle anchored aramid nanofiber (ANF) aerogel for superior microwave absorption capacity†

Xin Hao [ID] *

High-efficiency, porous and renewable magnetic microwave absorbing (MA) materials have been enthusiastically pursued due to their suitable impedance matching, light weight, strong multiple scattering and the synergy effect of dielectric and magnetic loss. Herein, a three-dimensional (3D) Co@C/ANF aerogel, composed of magnetic MOF derivatives embedded in biomass aramid nanofiber (ANF), was prepared for the first time through a directional-freezing method followed by an annealing process. To evaluate their MA attenuation performance, the electromagnetic parameters of Co@C/ANF composites with different component ratios were measured at 2–18 GHz. Profiting from the preserved porous structure of MOF derivatives, the construction of multiple heterogeneous interfaces and suitable electromagnetic parameters, Co@C/ANF 2 : 1 exhibited a good MA performance of $RL_{min} = -64.3$ dB (indicating more than 99.99996% microwaves were absorbed) and $EAB_{max} = 6.8$ GHz. Considering the admirable overall performance, the Co@C/ANF aerogel is deemed to be a promising candidate for the next-generation of lightweight, reproducible, and high-performance MA materials.

## Introduction

With the advent of the information age, electronic devices are widely used in various fields which greatly facilitates people's daily lives but leads to serious electromagnetic pollution, which not only interferes with the use of electronic devices but also seriously endangers human health.[1–5] To address this issue, researchers have been trying to find high-performance microwave absorbing (MA) materials with the characteristics of lightweight, strong absorption capacity and wide absorption band with small thickness to effectively absorb undesired microwaves.[6,7] In the past few decades, different types and microstructures of dielectric or magnetic materials have been designed as MA materials.[8–12] Nevertheless, consider that microwave is a vector entangled body that contains alternating electric and magnetic waves, the combination of magnetic and dielectric materials has increasingly become a mainstream.[13–15]

Recently, 3D metal organic frameworks (MOFs) composed of metal ions/clusters and organic ligands, with large specific surface area and adjustable microstructure, has widely received attention in gas storage, supercapacitors, batteries, information storage and sensors.[16–18] Typically, in MA materials field, porous magnetic MOFs derivatives (products of MOF after annealing or other treatments) can also play an obvious role. Especially, the

shape of the polyhedron can cause multiple reflections, and the microwave injected into the hollow MOF hole can increase the transmission path and the probability of being fully absorbed, so as to obtain a strong absorbing performance. For example, Lü *et al.* prepared porous Co/C composite nanomaterials, through annealing ZIF-67 at different temperatures, with the $RL_{min}$ of Co/C-500 is −35.3 dB and an effective absorption bandwidth (EAB) = 5.80 GHz.[19] The excellent MA performance confirms the feasibility of MOF derivatives as a MA material. Subsequently, Wang *et al.* introduced an inorganic shell outside the MOF derivative, which reduced the incident resistance of microwaves, resulting $SnO_2/Co_3Sn_2$@C hybrid can receive an optimal $RL_{min}$ value of −56.2 dB.[20] Nevertheless, the problem of high content (30 wt%) caused by the possible agglomeration of magnetic MOF derivative materials in matrix still needs to be further solved. Hopefully, Ji *et al.* used melamine foam as the skeleton of MOF derivatives to prepare a 3D porous network structure, and the obtained microwave absorption effect can be increased to the $RL_{min}$ value of −59.82 dB.[21] In addition, the hybrid aerogel also has excellent infrared invisibility and heat insulation, revealing the bright future of MOF derivatives/ aerogel multifunctional MA materials. Therefore, choosing a key dielectric material as the 3D framework of the magnetic MOF derivative can rich the polarization site of the microwave, the scattering interface and the synergistic loss effect of aerogel, and it is an effective means for designing high-efficiency MA materials.

Aramid nanofibers (ANF) is a promising candidate to have great application potential for next-generation pollution-free

*International College, Zhengzhou University, Zhengzhou, Henan Province, 450000, P. R. China. E-mail: haoxinzzu@163.com*

materials with excellent thermal conductivity, renewable and biocompatible.[22–24] Since uniformly dispersed ANF was first prepared by Kotov and co-workers, due to its high porosity, large specific surface area, high aspect ratio, unique nanoscale effects and higher mechanical strength than CNF, it has been widely used in many emerging fields such as thermal conductivity, EMI shielding and energy, *etc.* Theoretically, aerogels benefiting from the combination of porous and dielectric biomass cellulose and MOF derivatives can effectively introduce microwaves and gradually attenuate them through multiple reflections. However, as far as well know, there are few reports on the application of ANF in microwave absorption, especially MOF derivatives/ANF aerogel EM material.

In this work, Co@C/ANF aerogel was successfully fabricated through the gentle ammonia annealing process using ZIF-67/ANF composite as a precursor. Subsequently, by changing the ratio of ZIF-67 to ANF, the electromagnetic parameters of Co@C/ANF were well adjusted, which affected the overall absorbing performance of the aerogel. As expected, with multiple heterogeneous interfaces, hierarchical pore structure, dielectric and magnetic loss effects, the results indicate that Co@C/ANF 2 : 1 can possess outstanding MA performances of $RL_{min} = -64.3$ dB at 3.5 mm and an $EAB_{max}$ of 6.8 GHz. Taking the lightweight aerogel structure of Co@C/ANF, excellent environmental friendliness and strong wave absorbing performance into account, this work opened up a new journey in the design of ANF-based magnetic MA materials.

# Experimental

## Materials

Poly-*p*-phenylene terephthamide (PPTA) fibers were purchased from DuPont Co., Ltd. (China). 2-Methylimidazole, cobalt chloride hexahydrate ($CoCl_2 \cdot 6H_2O$), potassium hydroxide (KOH), methyl alcohol ($CH_3OH$), and dimethyl sulfoxide (DMSO) were purchased from Aladdin Co., Ltd. (China, Shanghai) and used without further purification.

## Preparation of the ZIF-67

The synthesis of ZIF-67 was prepared *via* the previously reported method.[25] 291 mg $CoCl_2 \cdot 6H_2O$ and 328 mg 2-methylimidazole were dissolved in 25 ml of methanol, respectively. After that, the mixture was stirred for 10 min and left for 24 h. Subsequently, the wash products were separated by centrifugation and dried overnight at 60 °C to obtain ZIF-67.

## Preparation of the Co@C/ANF composite

The fabrication progress of the Co@C/ANF composite is illustrated in Scheme 1. Typically, 7.5 g PPTA and 9 g KOH were added into 500 ml DMSO with stirring for one week at room temperature. After that, a dark red-brown solution was obtained. Subsequently, the obtained ZIF-67 and ANF were mixed in the mass ratio of 1 : 2, 1 : 1, and 2 : 1, respectively. Then directed frozen and lyophilized. Finally, Co@C/ANF composites were obtained by calcination under a flowing ammonia atmosphere at 500 °C for 2 h (5 °C min$^{-1}$).



**Scheme 1** The fabrication process of Co@C/ANF aerogel.

## Characterization

The structure of the samples was verified by Fourier transform infrared spectroscopy (FTIR, Nicolet 6700), X-ray powder diffraction (XRD, Cu Kα, 5–90°, Ultima IV), and Raman spectroscopy. The morphology of the synthesized materials was determined by scanning electron microscopy (SEM, JSM-7001F) and transmission electron microscopy (TEM, JEOL JEM-2100F). The surface components of the samples were analyzed on an X-ray photoelectron spectroscopy (XPS Thermo Scientific K-Alpha XPS). The magnetic properties of the samples were measured using a vibrating sample magnetometer (VSM, LakeShore 7404). The relative permeability and permittivity were obtained on a vector network analysis (VNA, Agilent 5234A) at the range of 2–18 GHz. The samples were prepared by dissolving PVDF in DMF, and then the synthetic Co@C/ANF composite was ultrasonically dispersed into PVDF and pressed into a ring with an inner diameter of 3.04 mm and an outer diameter of 7.00 mm.

# Results and discussion

The morphology of the different composites was analyzed by SEM. As shown in Fig. 1a, the synthesized ZIF-67 revealed a well-defined dodecahedron structure, which shows the stability of the synthesis strategy. As a derivative of ZIF-67, Co@C will
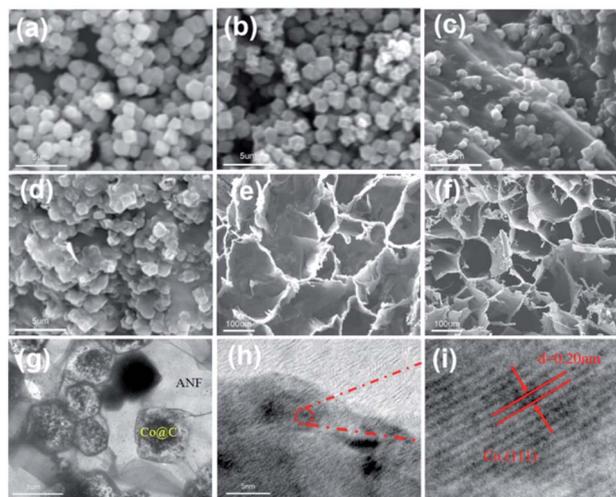


**Fig. 1** SEM images of (a) ZIF-67, (b) Co@C, (c) ZIF-67/ANF aerogel, (d) Co/C@ANF aerogel and the top-view of (e) ZIF-67/ANF and (f) Co@C/ANF aerogel. (g) TEM images and (h, i) HRTEM images of Co/C@ANF.

slightly decrease its volume due to the removal of ligands and the adding of a large number of pores on the surface (Fig. 1b). Furthermore, benefiting from the effective dispersion of ZIF in the ANF solution, ZIF-67 nanoparticles were uniformly mounted or embedded in the surface of ANF (Fig. 1c) indicating the ZIF-67 was well anchored on ANF in the freeze-dried ZIF-67/ANF aerogel. After annealing, in Fig. 1d, Co@C/ANF aerogel changed a little after calcination and some concave shape appeared on the particle surface, which may be due to the loss of organic components and the anisotropic field driving the growth of cobalt particles at elevated temperatures. Detailly, the cross-sections SEM of ANF, ZIF-67/ANF and Co@C/ANF before and after annealing are shown in Fig. S1 and S2 (ESI†). Interestingly, the surface of the annealed aerogel appears smoother, which may be due to the carbonization of the surface and the removal of impurities. Correspondingly, the top views of ZIF-67/ANF and Co@C/ANF were shown in Fig. 1e and f, respectively, confirming that the porous structure of the aerogel is well preserved before and after annealing.

The TEM result further proves the internal microstructure of Co@C/ANF aerogel. As shown in Fig. 1g, the microframes retained the ZIF-67 shapes, confirmed the formation of core–shell structures of Co@C polyhedral particles and embedded onto ANF nanosheets. The high-resolution TEM images are shown in Fig. 1h and i. It can be found that the lattice fringe of 0.20 nm for encapsulated nanoparticles core corresponds to the well-resolved (111) lattice plane of Co nanoparticle, indicating a core–shell structure composed of cobalt nanoparticle cores and carbon nanosheet shells was successfully prepared, which is consistent with the SEM pattern results.

XRD analyses were used to confirm the crystalline structure and the constituents of the Co@C/ANF samples. As shown in Fig. 2a, the ZIF-67/ANF composite inherits the diffraction peaks of ZIF-67 and ANF (Fig. S3a, ESI†) completely. The ZIF-67 XRD pattern can be assigned to (011), (002) (112), and (222) crystal planes, which matches well with previous reports, proving the

successful synthesis of ZIF-67.[26,27] For the Co@C/ANF aerogel, the disappeared characteristic peak of ZIF-67 indicating the change in the crystal structure of ZIF-67 during calcination. The emerging four peaks in the Co@C/ANF composite at 44.2°, 51.5°, and 75.8° can be assigned to the (111), (200), and (220) crystal planes of cobalt metal (PDF# 15-0806), implies the formation of Co nanoparticles. Besides, the Co@C/ANF aerogel still retains the previous characteristic peaks of the calcined ANF, which can be speculated that the structure of ANF was reserved. To further confirm the changes in the composites, XPS analysis was used to analyze the chemical composition of ZIF-67/ANF and Co@C/ANF. The results confirmed the presence of C, N, C, O, and K elements in the samples (Fig. 2b). Interestingly, weak K $2p^3$ and N 1s peaks in ZIF-67/ANF can be observed at 293 eV and 401 eV, respectively, which is due to the use of KOH in the preparation of ANF and exist of N element in ANF. Precisely, Co@C/ANF shows the increasing N atom ratio, which implies a large amount of N atoms doping and defects are introduced during the annealing process. In Fig. S3 (ESI†), the prominent peaks at 398.5 and 400.5 in the N 1s spectrum reveal the formation of pyrrole nitrogen and pyridine nitrogen. Moreover, the C 1s signals at binding energies of 284.8 and 285.6 are attributed to C=C and C–N.[25] As for the specific chemical valence state of the element Co, the signals located at 778.3 eV and 793.5 eV can be attributed to $2p_{3/2}$ and $2p_{1/2}$ of Co, respectively, and the peaks at 781.5 eV and 796.4 eV correspond to the satellite peaks.[28] The XPS spectrum of Co element once again shows the formation of Co metal crystal particles, which is consistent with the XRD results.

FT-IR analysis was performed to characterize the change of functional groups before and after transformation of aerogels. Evidently, there is a broad peak at 3437 cm$^{-1}$ that corresponded to the –OH in the curve (Fig. 2c). In addition, the Co@C/ANF aerogel shows distinct bands at 1653, 1380, and 1129 cm$^{-1}$, which are correspond to C=O, N–H, and C–N, respectively, shows a similar peak to ZIF-67/ANF. The presence of oxygen/nitrogen-containing carbon bonds indicates that the annealed aerogel still retains some functional groups, which is conducive to the loss of dipolar polarization in the alternating electromagnetic field. Fig. 2d shows the magnetization hysteresis lines of ZIF-67/ANF and Co@C/ANF aerogels, where ZIF-67/ANF composite shows an almost flat line, indicating its non-magnetism property. On the contrary, the hysteresis curve of the ANF/MOF composite shows a typical ferromagnetic behavior, giving the hybrid material magnetic loss capability. Intriguingly, the Co@C/ANF composite exhibits a higher Hc (830 Oe), which can facilitate the natural resonance and enhance the magnetic loss of MA performance.

Generally, the MA property can be estimated from the reflection loss curve. According to transmission line theory, the value of RL can be calculated by the following equation.[29–31]

$$Z_{in} = Z_0 \sqrt{\frac{\mu_r}{\varepsilon_r}} \tanh\left[j\left(\frac{2\pi \pi f}{c}\right)\right] \sqrt{\mu_r \varepsilon_r} \quad (1)$$

$$RL \text{ (dB)} = 20 \log|(Z_{in} - Z_0)/(Z_{in} + Z_0)| \quad (2)$$
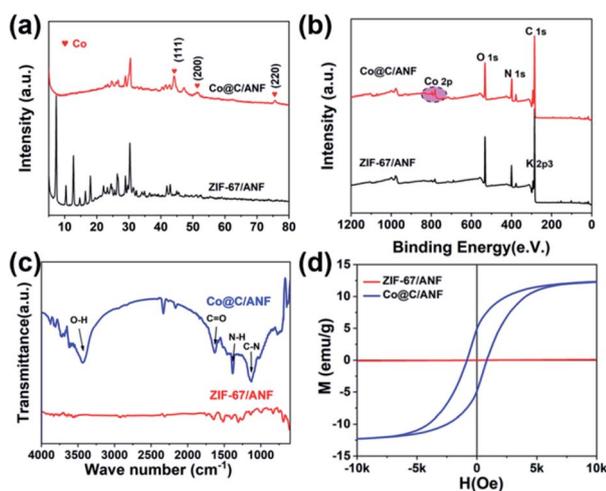


Fig. 2 (a) XRD patterns of Co@C/ANF and ZIF-67/ANF. (b) XPS spectra of Co@C/ANF and ZIF-67/ANF. (c) FT-IR spectra of Co@C/ANF. (d) Hysteresis loops of Co@C/ANF and ZIF-67/ANF.

where $Z_{in}$ represents the input characteristic impedance; $Z_0$ is the characteristic impedance in free space; $\varepsilon_r$ and $\mu_r$ are the complex permittivity and composite permeability, respectively; $d$ is the thickness and $c$ means the velocity of microwave in free space. As is well known, requiring RL < −10 dB, which means that more than 90% of the incident microwave radiation will be effectively absorbed, corresponding to the effective absorption bandwidth (EAB).[34]

The MA behavior of the Co@C/ANF aerogel was investigated in the frequency range of 2–18 GHz. Fig. 3 shows the RL curves of ANF and Co@C/ANF aerogels with different thicknesses. Overall, it is first observed that the peak frequency of the RL curves shifts to the lower frequency region with an increased thickness of the absorber, which can be explained by the quarter-wavelength ($\lambda/4$) cancelation theory.[32,35] Simultaneously, it can be found that the synthesized Co@C/ANF aerogels have significant performance advantages over pure ANF MA materials in Fig. 3a ($RL_{min}$ = −22.37 dB). With the content of MOF derivatives increased, according to Fig. 3b, it can be observed that the $RL_{min}$ value of Co@C/ANF 1 : 2 was −37.9 dB with EAB of 4.7 GHz. For the Co@C/ANF 1 : 1, the $RL_{min}$ value is −30.4 dB at 2.5 mm (Fig. 3c). Particularly, Fig. 3d shows that Co@C/ANF 1 : 2 exhibits an excellent MA characteristic and the $RL_{min}$ value can reach −64.3 dB at 3.5 mm. Intuitively, the 3D and 2D absorbing effects of the Co@C/ANF 2 : 1 are shown in Fig. 3e and f, respectively. By changing the thickness, the $RL_{min}$ of Co@C/ANF 2 : 1 can achieve an $EAB_{max}$ of 6.8 GHz at 2.5 mm. Through the comparison with the materials in the literature (Table 1), the advantages of Co@C/ANF 2 : 1 are further highlighted. Considering the overall MA capacity, it can be concluded that Co@C/ANF 2 : 1 exhibits the best MA performance with small $RL_{min}$, thin thickness, and wide EAB.

According to the energy conversion principle, the MA property is strongly related to relative complex permittivity ($\varepsilon_r = \varepsilon' - j\varepsilon''$) and the complex permeability ($\mu_r = \mu' - j\mu''$).[36] Specifically, the $\varepsilon'$ and $\mu'$ are mainly associated with the storage capacity of microwave energy, and the $\varepsilon''$ and $\mu''$ are connected with the dissipation capability of electrical and magnetic energy.[33,37] From Fig. 4a, it can be found that $\varepsilon'$ values gradually decrease from 11.5 to 4.2 for different samples. In an alternating electromagnetic field, the existence of a heterogeneous interface will cause electrons to shift and polarization will occur. However, as the frequency increases, when the polarization cannot keep up with the frequency, the real part of the dielectric constant will decrease, which explains the change in the dielectric constant. Besides, as shown in Fig. 4b, the Co@C/ANF composites present a lower value of $\varepsilon''$ compared to ANF. Due to the addition of ZIF-67, the conductive path of ANF is isolated, then the resistivity of Co@C/ANF composite is higher compared to ANF and this phenomenon can be explained by the free-electron theory ($\varepsilon'' \approx 1/2\pi\varepsilon_0\rho$). Moreover, several resonance peaks can be observed on the $\varepsilon''$ curve (Fig. 4b), proving the presence of multiple polarization relaxation in the composite. Based on the free-electron theory and the Debye theory, the relationship between $\varepsilon'$ and $\varepsilon''$ can be expressed by the following equation.[38,39]

$$\left(\varepsilon' - \frac{\varepsilon_s + \varepsilon_\infty}{2}\right)^2 + (\varepsilon'')^2 = \left(\frac{\varepsilon_s - \varepsilon_\infty}{2}\right)^2 \tag{3}$$

Fig. S4† shows the curves of $\varepsilon'$ and $\varepsilon''$, where a single semi-circle is denoted as a Cole–Cole semicircle, and if the curves form a semicircle it represents that a relaxation process may occur.[40] It can be seen that various multiple semicircles and small tail appear in the $\varepsilon'$–$\varepsilon''$ curves of Co@C/ANF samples, indicating that polarization relaxation contributed to their MA absorption performance, and conductance loss mechanism is exist. In addition, the Cole–Cole semicircles in these samples overlap and are distorted, which indicating that other mechanisms, such as Maxwell–Wagner relaxation and electron polarization, also contribute to the dielectric properties in addition to the Debye relaxation.[41,42]

For the complex permeability, the $\mu'$ and $\mu''$ values for samples exhibit a similar trend in 2–18 GHz. Fig. 4c and d show the magnetic permeability of different samples, although more ZIF-67 (Co@C/ANF 2 : 1) achieve a high magnetic permeability, the magnitude of the magnetic permeability between different samples is not large. As we know, for the magnetic materials, magnetic losses are mainly attributed to natural resonance, eddy current effect, and domain wall resonance. The eddy current loss caused by the eddy current effect can be expressed as $C_0$.[43,44] If the value of $C_0$ is the dominant factor causing the magnetic loss, then $C_0$ remains constant over the entire frequency range. However, significant fluctuations were detected in the $C_0$ curves for all samples, suggesting that the
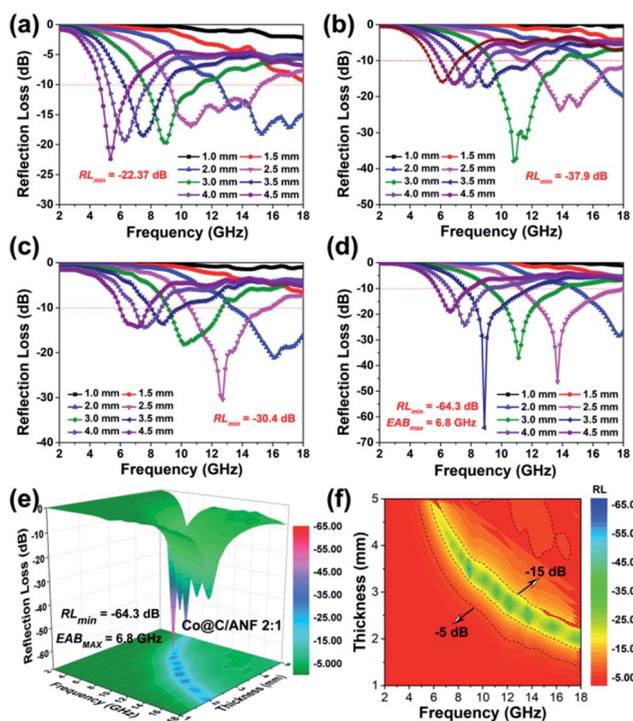


**Fig. 3** Reflection loss curve of (a) ANF (b) Co@C/ANF 1 : 2 and (c) Co@C/ANF 1 : 1 at 2–18 GHz. (d) 2D, (e) 3D and (f) flat reflection loss graph of Co@C/ANF 2 : 1.

**Table 1** Comparison of Co@C/ANF absorbing performance with other materials in literature

| Material name | Matrix | Filler loading (wt%) | Thickness (mm) | $RL_{min}$ (dB) | EAB (GHz) | Ref. |
|---|---|---|---|---|---|---|
| Fe–Co/NC/RGO | Wax | 25 | 2.5 | −33.26 | 9.12 | 2 |
| ZIF-67@CoNi | Wax | 30 | 2.5 | −58.2 | 4.03 | 13 |
| Fe–Co/NPC | Wax | 50 | 1.2 | −21.7 | 5.8 | 15 |
| Ni@C-ZIF | Wax | 40 | 2.7 | −86.8 | 7.4 | 17 |
| FeCoNi@C | Wax | 38 | 2.1 | −64.75 | 8.08 | 18 |
| Co/C | Wax | 40 | 2.5 | −35.3 | 5.80 | 19 |
| $Co_{1.29}Ni_{1.71}O_4$ | Wax | 50 | 1.6 | −50.7 | 4.84 | 30 |
| $Fe_3O_4$/CNT | Wax | 30 | 8.3 | −28.7 | 1.75 | 32 |
| $CS/MoS_2$ | Wax | 30 | 1.4 | −52.6 | 4.9 | 33 |
| Co@C/ANF 2 : 1 | PVDF | 10 | 3.5 | −64.3 | 4.5 | This work |
| Co@C/ANF 1 : 2 | PVDF | 10 | 2.5 | −46.3 | 6.8 | This work |
| Co@C/ANF 1 : 1 | PVDF | 10 | 3 | −37.9 | 4.8 | This work |
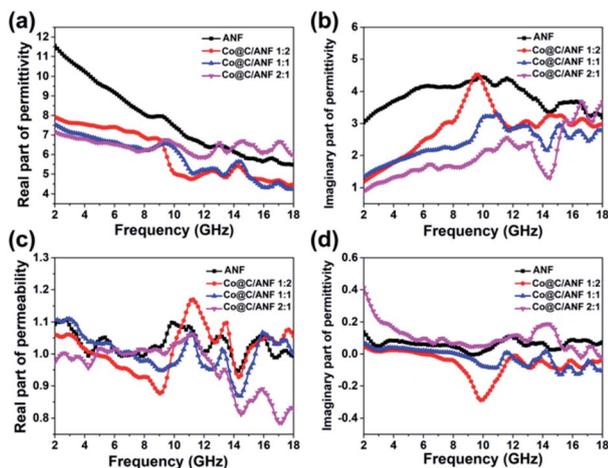


**Fig. 4** Frequency dependence of (a) real part and (b) imaginary part of the relative complex permittivity. (c) Real part and (d) imaginary part of the relative complex permeability of Co@C/ANF aerogels.

magnetic losses are mainly caused by exchange resonance and natural resonance effects (Fig. S5a, ESI†).

Dielectric loss angle tangent and magnetic loss angle tangent are two important factors to evaluate the absorbing performance of MA materials. According to $\varepsilon'$ $\varepsilon''$ $\mu'$ and $\mu''$, the curves of dielectric loss angle tangent and magnetic loss angle tangent can be obtained by using the following equations $\tan \delta_\varepsilon = \varepsilon''/\varepsilon'$ and $\tan \delta_\mu = \mu''/\mu'$. As displayed in Fig. 5, it is obvious that the $\tan \delta_\varepsilon$ values of all composites are far larger than the $\tan \delta_\mu$ values, showing that dielectric loss plays a dominant role in the composite absorber. In general, the higher the value of dielectric loss angle tangent, the more electric energy of incident microwave can be dissipated. Compared to other samples, Co@C/ANF 2 : 1 shows a higher $\tan \delta_\varepsilon$ values. This should originate from its high $\varepsilon''$ value at 8–12 GHz, confirming that the Co@C/ANF 2 : 1 has a more outstanding dielectric loss performance at 8–12 GHz. However, Fig. S5b (ESI†) exhibits that $\tan \delta_\varepsilon$ + $\tan \delta_\mu$ of pure ANF is larger than that of the Co@C/ANF composites, which means that the combined microwave loss capability of the composite is lower than that of ANF.

To further investigate the MA mechanism of Co@C/ANF, the attenuation coefficient and impedance matching should be introduced. Attenuation coefficient ($\alpha$) and impedance matching are the key factors affecting the absorbing performance of composite materials, which determine the entry capacity and inherent attenuation capacity in the microwave wave absorber.[45] As shown in Fig. 6a, within a certain range, ANF shows the highest $\alpha$ value in almost the entire frequency. This may be because of its high values of $\varepsilon''$. Although the loss capability of pure ANF is stronger than the Co@C/ANF composite, on the whole, they both have high $\tan \delta_\varepsilon$ + $\tan \delta_\mu$ values and attenuation constants and maintain a strong MA capability.

Generally, as the ratio of the input impedance of the absorber to the free space impedance ($|Z_{in}/Z_0|$) is equal to 1, most of the microwaves can easily enter the absorber, which helps to improve the MA performance.[46] The impedance matching of the Co@C/ANF 2 : 1 sample vs. frequency is presented in Fig. 6b, and it can be found that the impedance matching of Co@C/ANF 1 : 2 is close to 1. Therefore, for the Co@C/ANF 2 : 1, microwave can be easily incident into the
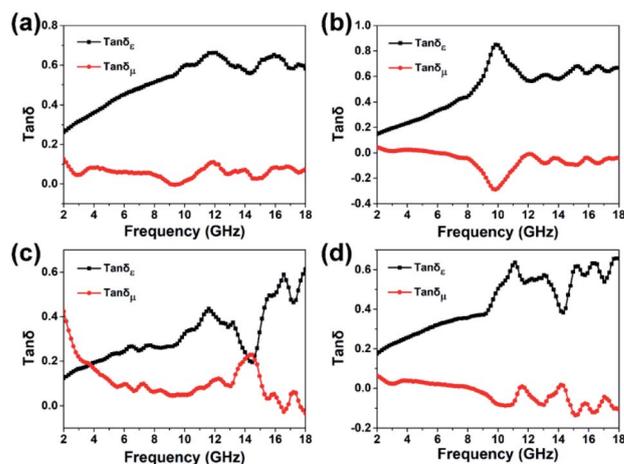


**Fig. 5** The loss angle tangent and the magnetic loss angle tangent of (a) ANF, (b) Co@C/ANF 1 : 2, (c) Co@C/ANF 1 : 1 and (d) Co@C/ANF 2 : 1.
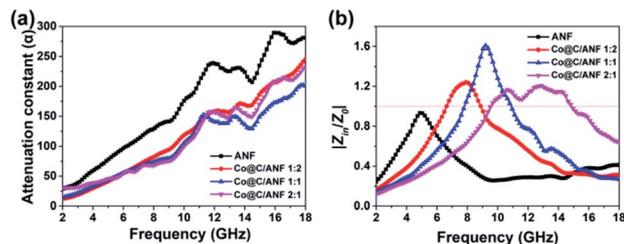
Fig. 6 (a) The attenuation constant and (b) the impedance matching of Co@C/ANF aerogels.

absorber then attenuated rather than reflected at the absorber surface. Interestingly, in the left point (around 10 GHz) of the impedance in Co@C/ANF 2 : 1 is equal to 1, but the optimal RL value cannot be obtained due to the weak attenuation capabilities. Therefore, it can be concluded that the appropriate impedance matching and strong attenuation capability are two important factors for obtaining excellent absorbing properties. Fig. S6 (ESI†) shows the impedance matching of the four samples at different thicknesses. These results demonstrate that excellent impedance matching is the first element for their excellent MA performance.

Based on the above discussions, the MA characteristics of Co@C/ANF composite are mainly determined by the following factors (Fig. 7): (i) the introduction of MOF derivative particles implies a higher resistance in the Co@C/ANF aerogel, leading to excellent impedance matching and resulting in more microwaves reaching the material.[47] (ii) The hollow-porous structure of Co@C/ANF composite extends the propagation range of incident waves, producing various reflection and scattering events that benefit the conversion of microwaves into other forms of energy.[48,49] (iii) The addition of a large amount of MOF derivative particles can bring more interfaces, leading to interfacial polarization and dipole polarization between MOF derivative and ANF, resulting in microwave energy attenuation.[50] For magnetic losses, eddy current effects and natural resonance play a major role in enhancing microwave absorption. Therefore, considering the excellent over all microwave attenuation capacity, Co@C/ANF 2 : 1 can be a promising and attractive absorber for application in the MA field.
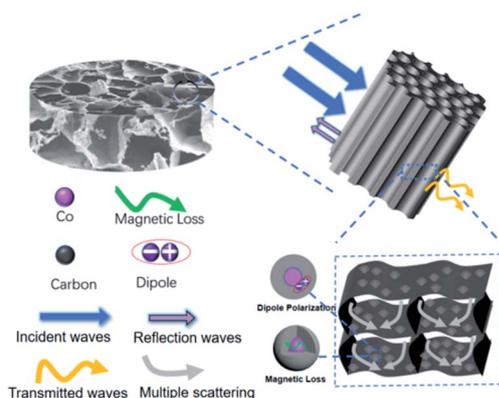


Fig. 7 Microwave absorbing mechanism of Co@C/ANF aerogel.

## Conclusions

In summary, Co@C/ANF composite was successfully synthesized using a facile pyrolysis of the ZIF-67 precursor and ANF. The morphology and structure of the aerogel of Co@C/ANF were characterized by SEM, TEM, FTIR, and XPS. MA performance test results demonstrated that, after annealing, Co@C content significantly affects the MA performance and shows better MA properties than pure ANF. In particular, Co@C/ANF 2 : 1 shows the best absorption performance with the $RL_{min}$ of $-64.3$ dB at a thickness of 3.5 mm, and the $EAB_{max}$ can reach 6.8 GHz by adjusting the thickness. In a word, Co@C/ANF composites have broadband, thin thickness, and strong MA characteristics, and have broad prospects in commercial and military fields.

## Conflicts of interest

There are no conflicts to declare.

## Acknowledgements

## Notes and references

1 H. Lv, Z. Yang, P. L. Wang, G. Ji, J. Song, L. Zheng, H. Zeng and Z. J. Xu, *Adv. Mater.*, 2018, **30**, 1706343.

2 S. Wang, Y. Xu, R. Fu, H. Zhu, Q. Jiao, T. Feng, C. Feng, D. Shi, H. Li and Y. Zhao, *Nano-Micro Lett.*, 2019, **11**, 76.

3 V. K. Rohith, P. Saravanan, K. T. R. Suresh, R. Radha, M. Balasubramaniam and S. Balakumar, *Nanoscale*, 2018, **10**, 12018–12034.

4 L. Liang, P. Xu, Y. Wang, Y. Shang, J. Ma, F. Su, Y. Feng, C. He, Y. Wang and C. Liu, *Chem. Eng. J.*, 2020, **395**, 125209.

5 S. L. Wen, Y. Liu and X. Zhao, *Adv. Powder Technol.*, 2015, **26**, 1520–1528.

6 P. Yang, X. Zhao, Y. Liu and Y. Gu, *J. Phys. Chem. C*, 2017, **121**, 8557–8568.

7 J. Liu, D. Zhu, C. Guo, A. Vasileff and S.-Z. Qiao, *Adv. Energy Mater.*, 2017, **7**, 1700518.

8 M.-S. Cao, Y.-Z. Cai, P. He, J.-C. Shu, W.-Q. Cao and J. Yuan, *Chem. Eng. J.*, 2019, **359**, 1265–1302.

9 J.-C. Shu, X.-Y. Yang, X.-R. Zhang, X.-Y. Huang, M.-S. Cao, L. Li, H.-J. Yang and W.-Q. Cao, *Carbon*, 2020, **162**, 157–171.

10 X. Zeng, X. Cheng, R. Yu and G. D. Stucky, *Carbon*, 2020, **168**, 606–623.

11 Y. Wang, D. Sun, G. Liu and W. Jiang, *Adv. Powder Technol.*, 2015, **26**, 1537–1543.

12 G. Wang, Y. Chang, L. Wang and C. Liu, *Adv. Powder Technol.*, 2012, **23**, 861–865.

13 Y. Zhao, W. Wang, J. Wang, J. Zhai, X. Lei, W. Zhao, J. Li, H. Yang, J. Tian and J. Yan, *Carbon*, 2021, **173**, 1059–1072.

14 Y. Yin, X. Liu, X. Wei, Y. Li, X. Nie, R. Yu and J. Shui, *ACS Appl. Mater. Interfaces*, 2017, **9**, 30850–30861.

15 X. Zhang, G. Ji, W. Liu, B. Quan, X. Liang, C. Shang, Y. Cheng and Y. Du, *Nanoscale*, 2015, **7**, 12932–12942.

16 X. Xu, F. Ran, Z. Fan, Z. Cheng, T. Lv, L. Shao and Y. Liu, *ACS Appl. Mater. Interfaces*, 2020, **12**, 17870–17880.

17 J. Yan, Y. Huang, Y. Yan, L. Ding and P. Liu, *ACS Appl. Mater. Interfaces*, 2019, **11**, 40781–40792.

18 J. Ouyang, Z. He, Y. Zhang, H. Yang and Q. Zhao, *ACS Appl. Mater. Interfaces*, 2019, **11**, 39304–39314.

19 Y. Lü, Y. Wang, H. Li, Y. Lin, Z. Jiang, Z. Xie, Q. Kuang and L. Zheng, *ACS Appl. Mater. Interfaces*, 2015, **7**, 13604–13611.

20 S. Wang, S. Peng, S. Zhong and W. Jiang, *J. Mater. Chem. A*, 2018, **6**, 9465–9474.

21 W. Gu, J. Tan, J. Chen, Z. Zhang, Y. Zhao, J. Yu and G. Ji, *ACS Appl. Mater. Interfaces*, 2020, **12**, 28727–28737.

22 F. Xie, F. Jia, L. Zhuo, Z. Lu, L. Si, J. Huang, M. Zhang and Q. Ma, *Nanoscale*, 2019, **11**, 23382–23391.

23 P. Hu, J. Lyu, C. Fu, W.-b. Gong, J. Liao, W. Lu, Y. Chen and X. Zhang, *ACS Nano*, 2020, **14**, 688–697.

24 Z. Ma, S. Kang, J. Ma, L. Shao, A. Wei, C. Liang, J. Gu, B. Yang, D. Dong, L. Wei and Z. Ji, *ACS Nano*, 2019, **13**, 7578–7590.

25 H. Chen, Z. Zhang, D. Hu, C. Chen, Y. Zhang, S. He and J. Wang, *Chemosphere*, 2021, **265**, 129047.

26 M. Abdul Nasir Khan, P. Kwame Klu, C. Wang, W. Zhang, R. Luo, M. Zhang, J. Qi, X. Sun, L. Wang and J. Li, *Chem. Eng. J.*, 2019, **363**, 234–246.

27 M. Yang, K. Cao, L. Sui, Y. Qi, J. Zhu, A. Waas, E. M. Arruda, J. Kieffer, M. D. Thouless and N. A. Kotov, *ACS Nano*, 2011, **5**, 6945–6954.

28 H. Zhao, Y. Cheng, J. Ma, Y. Zhang, G. Ji and Y. Du, *Chem. Eng. J.*, 2018, **339**, 432–441.

29 M. Green, Z. Liu, R. Smedley, H. Nawaz, X. Li, F. Huang and X. Chen, *Mater. Today Phys.*, 2018, **5**, 78–86.

30 D. Lan, M. Qin, J. Liu, G. Wu, Y. Zhang and H. Wu, *Chem. Eng. J.*, 2020, **382**, 122797.

31 B. Zhao, G. Shao, B. Fan, Y. Xie, B. Sun and R. Zhang, *Adv. Powder Technol.*, 2014, **25**, 1761–1766.

32 N. Li, G.-W. Huang, Y.-Q. Li, H.-M. Xiao, Q.-P. Feng, N. Hu and S.-Y. Fu, *ACS Appl. Mater. Interfaces*, 2017, **9**, 2973–2983.

33 F. Zhang, W. Zhang, W. Zhu, B. Cheng, H. Qiu and S. Qi, *Appl. Surf. Sci.*, 2019, **463**, 182–189.

34 L. Liang, R. Yang, G. Han, Y. Feng, B. Zhao, R. Zhang, Y. Wang and C. Liu, *ACS Appl. Mater. Interfaces*, 2020, **12**, 2644–2654.

35 G. Sun, B. Dong, M. Cao, B. Wei and C. Hu, *Chem. Mater.*, 2011, **23**, 1587–1593.

36 G. Wu, Y. Cheng, Y. Ren, Y. Wang, Z. Wang and H. Wu, *J. Alloys Compd.*, 2015, **652**, 346–350.

37 R. Qiang, Y. Du, H. Zhao, Y. Wang, C. Tian, Z. Li, X. Han and P. Xu, *J. Mater. Chem. A*, 2015, **3**, 13426–13434.

38 L. Yan, C. Hong, B. Sun, G. Zhao, Y. Cheng, S. Dong, D. Zhang and X. Zhang, *ACS Appl. Mater. Interfaces*, 2017, **9**, 6320–6331.

39 L. Wang, Y. Guan, X. Qiu, H. Zhu, S. Pan, M. Yu and Q. Zhang, *Chem. Eng. J.*, 2017, **326**, 945–955.

40 H. Lv, Y. Guo, G. Wu, G. Ji, Y. Zhao and Z. J. Xu, *ACS Appl. Mater. Interfaces*, 2017, **9**, 5660–5668.

41 B. Zhao, X. Guo, W. Zhao, J. Deng, G. Shao, B. Fan, Z. Bai and R. Zhang, *ACS Appl. Mater. Interfaces*, 2016, **8**, 28917–28925.

42 Y. Du, W. Liu, R. Qiang, Y. Wang, X. Han, J. Ma and P. Xu, *ACS Appl. Mater. Interfaces*, 2014, **6**, 12997–13006.

43 T. Wu, Y. Liu, X. Zeng, T. Cui, Y. Zhao, Y. Li and G. Tong, *ACS Appl. Mater. Interfaces*, 2016, **8**, 7370–7380.

44 K. Wang, Y. Chen, R. Tian, H. Li, Y. Zhou, H. Duan and H. Liu, *ACS Appl. Mater. Interfaces*, 2018, **10**, 11333–11342.

45 L. Liang, Q. Li, X. Yan, Y. Feng, Y. Wang, H.-B. Zhang, X. Zhou, C. Liu, C. Shen and X. Xie, *ACS Nano*, 2021, **15**, 6622–6632.

46 L. Liang, G. Han, Y. Li, B. Zhao, B. Zhou, Y. Feng, J. Ma, Y. Wang, R. Zhang and C. Liu, *ACS Appl. Mater. Interfaces*, 2019, **11**, 25399–25409.

47 H. Ren, J. Ma, Z. Zhu, Z. Liu, Y. Liu, L. B. Kong, F. Min and J. Zhu, *Adv. Powder Technol.*, 2021, **32**, 885–894.

48 Z. Li, X. Han, Y. Ma, D. Liu, Y. Wang, P. Xu, C. Li and Y. Du, *ACS Sustainable Chem. Eng.*, 2018, **6**, 8904–8913.

49 Q. Yang, Y. Shi, Y. Fang, Y. Dong, Q. Ni, Y. Zhu and Y. Fu, *Compos. Sci. Technol.*, 2019, **174**, 176–183.

50 F. Zhang, H. Du, S. Shang, M. Qaim, S. Bao, T. Su, R. Zhang, H. Lu, H. Wang, H. Xu and B. Fan, *Adv. Powder Technol.*, 2020, **31**, 4642–4647.